LANGMUIR

pubs.acs.org/Langmuir Article

# Destabilizing a Buoyant Multilayer Granular Raft by Heavy Grains: The Role of Inertia

Mohammad Javad Sayyari and Joshua B. Bostwick*

Cite This: *Langmuir* 2025, 41, 18403−18413

Read Online

ACCESS | Metrics & More | Article Recommendations

**ABSTRACT:** Buoyant multilayer granular rafts are seen in oceanography across many scales, from microplastic pollutants on the ocean surface to ice mélange in the arctic region, and are capable of supporting loads that would otherwise sink. This study investigates the load-carrying capacity of a buoyant multilayer granular raft subjected to dynamic deformation by heavy grains. Experiments are performed to quantify the critical number of heavy particles $N_c$ required to destabilize the raft, as it depends upon the particle and liquid properties and the inertia of the heavy particles. Two experimental loading protocols are utilized, (1) quasi-static and (2) inertial jet, which are distinguished according to the inertia or lack thereof and give rise to distinct destabilization morphologies. Destabilization occurs when the width of the particle cluster reaches a maximum, and this coincides with the turning point of a preferred bifurcation diagram. This critical width can be more than two times larger than for the quasi-static case than for the inertial jet case. A mathematical model is developed to predict $N_c$ for a buoyant multilayer raft, which compares well with our experimental observations and those from prior literature over 7 orders of magnitude.

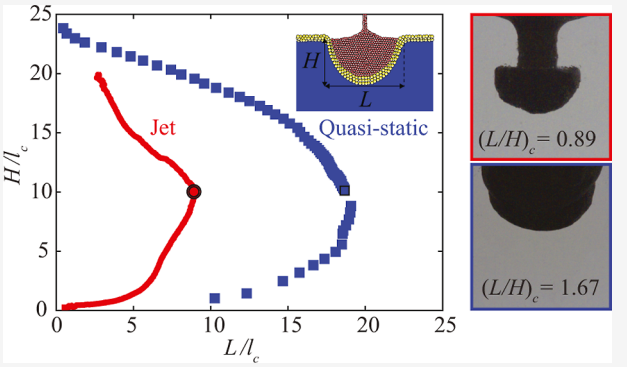




## INTRODUCTION

Granular rafts refer to the self-assembled close-packed monolayer of particles, with density larger than that of the liquid upon which it rests and size comparable to the capillary length.[1−3] Interparticle capillary forces are responsible for the enhanced load-carrying capacity of granular rafts compared to those of pure liquid interfaces.[4,5] This feature has been utilized in nature by fire ants to float on liquid surfaces during flood events.[6] Destabilization of a granular raft has been shown as an effective method for liquid transport through the creation of armored drops,[4] including stable aqueous water-in-water emulsions,[7] as well as armored bubbles.[8] The mechanical properties of a granular raft are often determined by the response to an external load, such as compression,[2] indentation by a rigid object,[9,10] drop impact,[11] and mechanical wave excitation.[12] These methods are summarized in the review by Protière.[2] In comparison to monolayer rafts, buoyant multilayer rafts have a greater capacity to support and transport heavier loads. A typical example of a buoyant multilayer raft is ice mélange seen in the arctic region, which has been modeled as a granular layer,[13] and is important to detectors in polar ocean regions,[14] the description of calving events at a glacier terminus,[15,16] landslides into fjords which cause damped surface waves,[17,18] and the transport of ice-rafted debris from shallow to deeper ocean waters.[19] In this paper, we performed a combined experimental and theoretical study to quantify the load-carrying capacity of a buoyant multilayer granular raft due to heavy grains focusing on the role of inertia.

Most prior literature focus on monolayer rafts as the simplest assembly for creating a granular boundary between liquid−liquid or gas−liquid interfaces to modify interfacial properties to, e.g., suppress evaporation.[20] However, in the real world, most granular rafts are not monolayer rafts and often consist of multiple layers of buoyant particles.[21,22] In the laboratory, it is challenging to control the assembly of particles and form monolayer rafts, especially for small particle sizes. The mechanical properties of a multilayer raft differ from a monolayer raft in that a multilayer raft consists of a wet layer in contact with the liquid that exhibits tensile strength due to capillary bridges between particles and a dry layer that exhibits compressive strength due to particle−particle interactions.[3,23] The situation becomes even more complicated when the particles are buoyant, which can further increase the load-carrying capacity compared to nonbuoyant particles.[3] The volume of literature on multilayer rafts and buoyant multilayer

Received: January 1, 2025
Revised: June 27, 2025
Accepted: July 1, 2025
Published: July 12, 2025

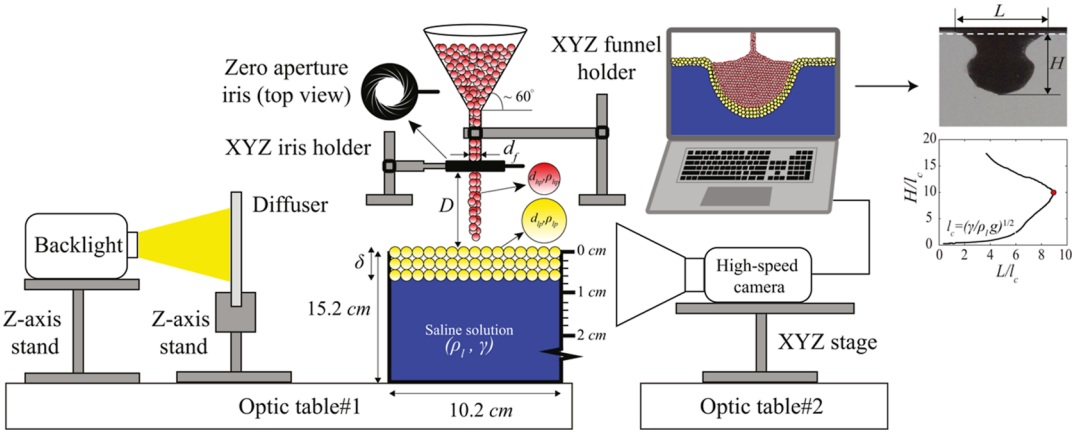


**Figure 1.** Experimental setup with typical experimental image (inset) showing raft destabilization.

rafts is comparatively small, despite their numerous applications in geophysical engineering.[21,24]

The buoyant layer can be classified as soft matter and is influenced by the energy of the impactor.[25] Therefore, the deformation, growth, and collapse of the raft depend on the properties of the load, in addition to those of the buoyant layer itself. This is supported by studies in the literature deforming an air−liquid interface, which demonstrate that the shape of the load is important,[26] the deposition geometry determines how many heavy particles can be supported,[27] and the energy of the impactors determines whether the granular stack collapses as a single lump or as a granular jet.[28] Here, we deform the buoyant multilayer raft by heavy grains, which imposes some unique features that affect the dynamics of the assembly compared to the cases where one of them does not have a granular structure. The heavy grains both deform the buoyant layer and build up on top of each other into a particle cluster whose maximum size is limited by wicking or breakup, which depends upon the Bond number.[1] In our experiment, wicking does not occur because the buoyant layer is composed of hydrophobic particles and protects the heavy grains from coming into direct contact with the liquid.

Dynamic loading introduces inertial effects, and this is also true for the granular jet of heavy particles we use in our experiments. Granular jets have been used in studies of impact onto a solid surface.[29,30] In our experiments, the deformability of the granular raft effectively constrains the impacting particles, leading to much smaller particle dispersion and a more uniform global deformation of the raft. The effects of deformability of the granular raft is readily seen when comparing the drop impact on a granular raft[7] to a granular bed[25] or a solid substrate.[31] The differences are significant. Furthermore, Planchette et al.[11] demonstrated the drop velocity required to rupture an armored liquid puddle increases with the particle size for mobile particles and decreases with the particle size for immobile particles.

We have developed a mathematical model to predict the load-carrying capacity of a buoyant multilayer granular raft by extending the model of Jones et al.[27] Our generalization includes additional dimensionless parameters and most importantly the inertia of the impacting particles. We have ignored the viscosity force of the liquid as Ong et al.[1] found that viscosity does not change the maximum stack depth. Following Protière et al.[32] and Jambon-Puillet et al.,[7] we idealize the buoyant multilayer as consisting of two distinct continuum sheets with effective properties for the wet and dry layers and write down a force balance which couples the interface shape and raft tension. Our model predictions compare favorably to our experimental observations, as well as prior experiments,[1,27] and limiting cases reproduce prior theoretical predictions.

We begin this paper by describing our experimental apparatus, protocols, and image processing techniques. Next, we present our experimental findings and derive a mathematical model to predict the critical load before collapse. We then compare our theoretical predictions to all relevant experimental data. We conclude by offering remarks contextualizing our results and on future directions. With regard to nomenclature, while "rafts" generally refer to monolayer rafts in the literature, we have also used this term for multilayer rafts, as well as the "buoyant layer". Additionally, "grain" and "particle" are used interchangeably. The terms "cluster", "stack", and "lump" all refer to the assembly of light and heavy particles. Lastly, "buoyant particles" and "light particles" are used interchangeably.

## EXPERIMENT

Experiments are performed using the setup shown schematically in Figure 1. A glass tank is filled with a saline solution of prescribed salt concentration, 0% w/w, 10% w/w, and 20% w/w. The density $\rho_l$ and surface tension $\gamma$ of the solution are given in Table 1. Light spherical polystyrene particles (Glen Mills Corp.) with diameter $d_{lp}$ and density $\rho_{lp} = SG_{lp}\rho_w$, with SG being the specific gravity, are deposited evenly on the liquid interface until the tank is filled to the brim, resulting in a buoyant layer of thickness $\delta$ in the range $1 \leq \delta \leq 5$ mm. Excess particles are gently removed from the buoyant layer using a piece of rigid paper to ensure a flat interface. The light polystyrene particles are slightly heavier than water yet remain

**Table 1. Liquid Properties of the Saline Solution, Including Density $\rho_l$ and Surface Tension $\gamma$, as it Depends upon Salt Concentration**

| salt concentration by mass [%] | density $\rho_l$ [kg/m$^3$] | surface tension $\gamma$ [mN/m] |
|---|---|---|
| 0 | 986.2 | 71 |
| 10 | 1061.2 | 76 |
| 20 | 1118.4 | 80 |


https://doi.org/10.1021/acs.langmuir.5c00012
Langmuir 2025, 41, 18403−18413

buoyant on our saline solutions and are hydrophobic, which prevents wicking and ensures the buoyant layer is largely dry.[33]

Heavy spherical particles with diameter $d_{hp}$ and density $\rho_{hp} = SG_{hp}\rho_w$ are introduced to the buoyant layer through a funnel located at a distance $1 \leq D \leq 4$ cm above the surface. Two types of heavy particles were used in our experiments and were made of polished glass ($SG_{hp}$ = 2.5, Sigmund Lindner) and zirconium oxide ($SG_{hp}$ = 3.8, Sigmund Lindner), respectively (cf. Table 2). Two protocols were used to load the buoyant

**Table 2. Particle Properties Including Diameter *d*, Specific Gravity SG, and Material**

| particle ID | diameter $d$ [$\mu$m] | specific gravity SG | material |
|---|---|---|---|
| LP1 | 168 ± 32 | 1.05 | polystyrene |
| LP2 | 296 ± 31 | 1.05 | polystyrene |
| LP3 | 370 ± 75 | 1.05 | polystyrene |
| LP4 | 763 ± 73 | 1.05 | polystyrene |
| LP5 | 1340 ± 340 | 1.05 | polystyrene |
| HP1 | 101.8 ± 27 | 2.5 | glass |
| HP2 | 283 ± 49 | 2.5 | glass |
| HP3 | 822.5 ± 104 | 2.5 | glass |
| HP4 | 1190.5 ± 89 | 2.5 | glass |
| HP5 | 1552.5 ± 91 | 2.5 | glass |
| HP6 | 150 ± 50 | 3.8 | zirconium oxide |
| HP7 | 250 ± 50 | 3.8 | zirconium oxide |
| HP8 | 700 ± 100 | 3.8 | zirconium oxide |
| HP9 | 1100 ± 100 | 3.8 | zirconium oxide |

layer with heavy particles, (1) quasi-static and (2) inertial jet, and these are distinguished by the inertia of the heavy particles or lack thereof. In the quasi-static protocol, heavy grains are introduced close to the interface with intermittent pauses to ensure that inertia is negligible. This process can take many minutes. In the inertial jet method, the heavy grains are initially blocked in the funnel using a zero-aperture iris, which is then opened, allowing the grains to flow continuously with the average mass flow rate $\dot{m}_{ave}$ and impact velocity $V_{imp}$. The inner diameter of the funnel tip $d_f$ = 4.32, 6.35, and 8.89 mm was chosen to produce a collimated particle jet that does not clog.[8] The mass flow rate of the heavy grains $\dot{m}_{ave}$ was measured by recording the time required for a known mass to discharge. Figure 2 plots $\dot{m}_{ave}$ against the particle diameter $d_{hp}$ for various combinations of particle density SG and funnel diameter $d_f$. Note there is a maximum for each curve, and this results from a balance between interparticle friction and packing density within the funnel.

The buoyant layer is deformed by the weight of the heavy particles into a typical shape, as shown in the inset of Figure 1. The collapse dynamics are captured in the side view by a Phantom VEO 410L high-speed camera at 3000 fps, equipped with a Nikon (Micro-NIKKOR 200 mm) lens. An optical diffuser (Edmund optics; Sandblasted Glass) is used to diffuse the backlight (Multiled LT-V9−15). Both the tank and camera are placed on separate optical tables to minimize interference. Each experiment is repeated at least three times. An in-house MATLAB code has been developed for image processing. Here, the image undergoes a morphological closing operation using disk-shaped structuring elements and binarization, with length calibration done using the outer diameter of the funnel tip. The interface shape is readily identified from the binarized image with edge detection, from which the height $H$, length $L$,

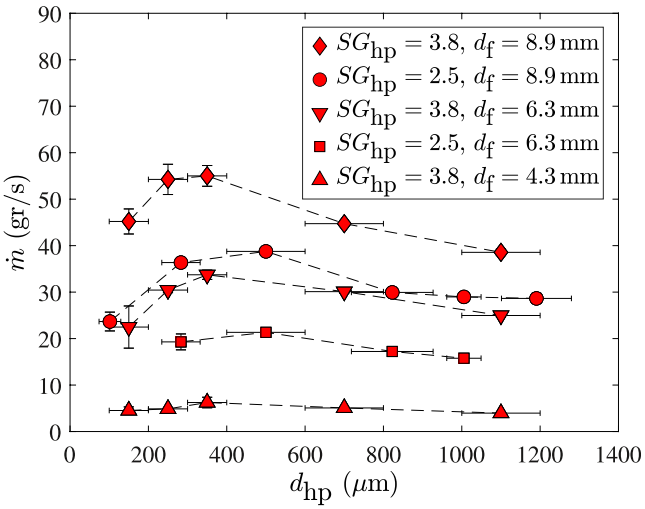


**Figure 2.** Average mass flow rate $\dot{m}_{avg}$ against heavy particle diameter $d_{hp}$, as it depends upon various combinations of funnel diameter $d_f$ and specific gravity SG.

cross-sectional area $A$, and vertical component of the center-of-mass $C_y$ are computed.

As a metric for load-carrying capacity, we experimentally determine the total number of heavy particles that cause collapse $N_c = \frac{M_c}{\rho_{hp}\mathrm{Vol}_{hp}}$, where $\mathrm{Vol}_{hp} = \frac{4}{3}\pi r_{hp}^3$ is the volume of a single spherical heavy particle. For the quasi-static protocol, the critical mass $M_c$ is measured gravimetrically by weighing the total mass of the heavy particles before and after collapse. For the inertial jet protocol, the critical mass can be approximated by multiplying the average mass flow rate by the total collapse time $t_c$, measured from the time at which the heavy particles touch the buoyant layer $M_c = \dot{m}_{ave}t_c$. Identifying the collapse time $t_c$ in experiment for the inertial jet protocol is not straightforward, and we will discuss our postprocessing techniques for determining it in the subsequent section.

## RESULTS

The buoyant layer is deformed through the loading of heavy grains and ultimately collapses when it is no longer able to support the load. The collapse dynamics strongly depend upon the loading protocol and whether the heavy particles carry inertia. Figure 3 contrasts the shape change dynamics of the buoyant layer for the two protocols: (a) inertial jet versus (b) quasi-static loading. Here, all experimental variables are held constant, with the exception of the mass flow rate for the inertial jet protocol. Comparing the initial stages of growth shows that quasi-static loading favors horizontal spreading, defined by the length $L$, whereas the inertial jet induces primarily vertical deformations defined by the height $H$. It is clear that the buoyant layer is able to support a larger load in the quasi-static case, as illustrated by the larger area $A$ shown in the critical panels (outlined in green line type) and as could be expected.

The morphology of destabilization differs greatly between the protocols. For the quasi-static case, the raft is gradually pulled down by the heavy particle, which is accompanied by an increase in the base radius that occurs until a protrusion appears (panel with $L/H$ = 3.22). This protrusion grows and becomes the source of destabilization when the base radius


https://doi.org/10.1021/acs.langmuir.5c00012
Langmuir 2025, 41, 18403−18413

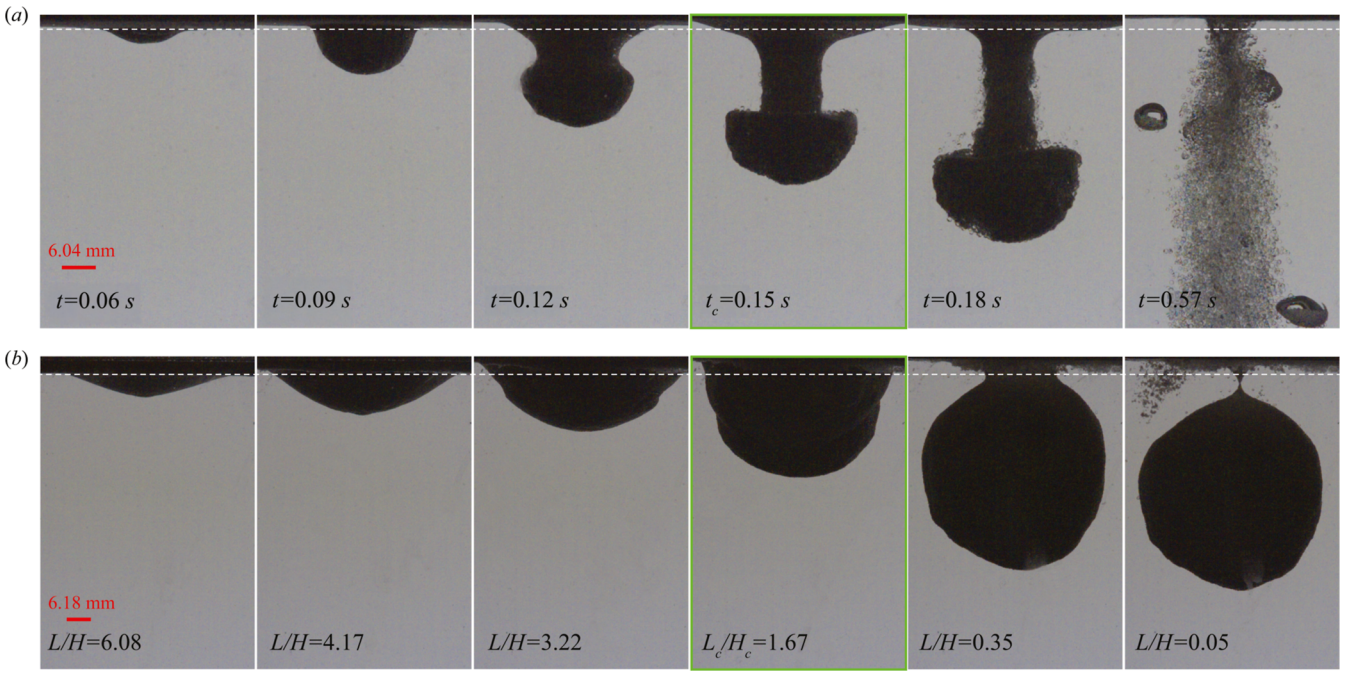


**Figure 3.** Evolution of a destabilizing buoyant layer contrasting (a) inertial jet and (b) quasi-static loading. Experimental conditions correspond to heavy particles HP3 loading a buoyant layer comprised of light particles LP1 with thickness $\delta$ = 3 mm on a saline solution of 10% w/w salt concentration. For inertial jet loading, the mass flow rate is $\dot{m}_{avg}$ = 29.9 g/s and funnel diameter $d_f$ = 8.9 mm. Here, the white dashed lines are the flat buoyant layer/liquid interface to guide the eye, the red lines are the scale bars, and the panels corresponding to the onset of collapse are shown with a green outline.

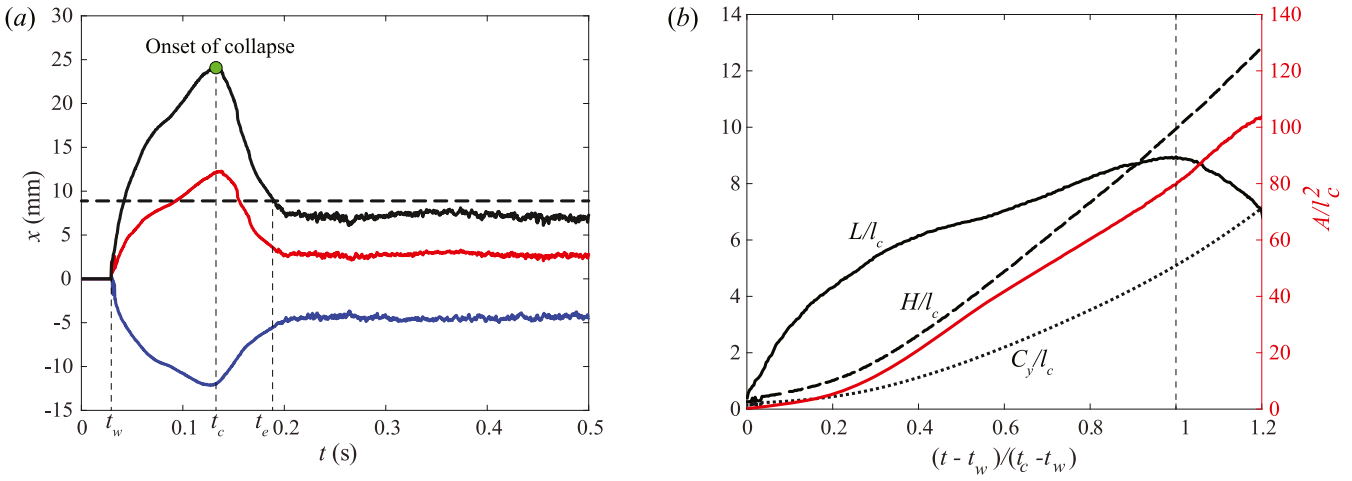


**Figure 4.** (a) Identification of the onset of collapse by plotting the time trace of the width $L = |x_R - x_L|$ defined by the left $x_L$ (blue) and right $x_R$ (red) foot locations, respectively. The green circle marks the onset of collapse. The horizontal dashed line is the inner diameter of the funnel (8.9 mm). (b) Dimensionless cluster properties, normalized by the capillary length $l_c$, including length ($L/l_c$, solid black line), depth ($H/l_c$, dashed line), $y$ component of the center-of-mass ($C_y/l_c$, dotted line), and area ($A/l_c^2$, red curve), as they depend upon dimensionless time $\hat{t} = (t - t_w)/(t_c - t_w)$.

reaches its maximum value (critical point, $L_c/H_c$ = 1.67), after which it shrinks inward forming a neck (panel with $L/H$ = 0.05) that thins and eventually ruptures, resulting in a cluster of heavy particles that sink to the bottom of the tank. We note that in some cases, multiple protrusions exist, giving rise to two necking regions which can rupture at the same time or with a small time delay. It is important to note that time is not a relevant factor here due to the pauses during the quasi-static loading protocol. For the jet case, the buoyant layer is forced to deform locally into a shape resembling a hemispherical cap, after which the cap transitions to a mushroom-shaped interface with a growing stem. We observe that the cap size becomes smaller as the density of the heavy particles increases, consistent with the observations of Ong et al.[28] The radius of the stem increases until reaching its maximum value at $t = t_c$, after which it begins to shrink until it approaches the inner radius of the funnel at time $t = t_e$, which we refer to as the end time, after which the jet comes into direct contact with the liquid, leaving a hole in the buoyant layer. For both protocols, there is a short amount of time, which we refer to as the waiting time, $t_w$, where the interface is not deformed despite being loaded by heavy particles. This is due to the initial resistance of the granular layer to deformation.[3]



https://doi.org/10.1021/acs.langmuir.5c00012
Langmuir 2025, 41, 18403−18413

Lastly, we note that air is introduced into the liquid through various mechanisms, including air entrainment, encapsulation of air in the pores, formation of an air cavity adjoining the falling grains, and the dragging of air into the liquid by the grains.[28] The trapped air, especially at the sides of the mushroom cap, gets released only after $t_e$ as granular bubbles that are partially coated with particles (see the panel of $t = 0.57$ s). Cervantes-Álvarez et al.[8] observed these trapped bubbles only when collimated granular jets, and not dispersed jets, enter directly into the liquid, consistent with our experimental observations. While the entrainment of gas is interesting, this is not the focus of our work.

Identification of the point of destabilization is straightforward for the quasi-static protocol but requires a metric to be defined by the inertial jet protocol. Here, we have chosen the base length $L = |x_R - x_L|$, as measured by the difference between the left $x_L$ and right $x_R$ foot, as this metric. Figure 4a plots the time trace of $L$ showing that a maximum is achieved at the onset of collapse $t_c$. Note that $L$ sits below the funnel diameter (thick dashed line) after $t_e$ when the jet is in direct contact with the liquid. This is attributed to the dynamics of the granular jet discharging from a hopper.[34] Figure 4b plots the geometric properties of the buoyant layer, as defined by the length $L/l_c$, depth $H/l_c$, vertical component of the center-of-mass $C_y/l_c$, and cross-sectional area $A/l_c^2$, all nondimensionalized with the capillary length $l_c = \left(\frac{\gamma}{g(\rho_l - \rho_{air})}\right)^{1/2}$, against dimensionless time $\hat{t} = \frac{t - t_w}{t_c - t_w}$. The critical properties occur at $\hat{t} = 1$. Here, we observe that $L$ and $H$ become nearly equal near the critical time, after which $H$ continues to increase while $L$ begins to decrease.

Buoyant layer destabilization is readily inferred from the preferred bifurcation diagram shown in Figure 5, which plots the normalized height $H/l_c$ against the normalized length $L/l_c$, contrasting the quasi-static (symbols) with the inertial jet (red line type) protocols. Here, the critical point is associated with the turning point of the preferred bifurcation diagram. For both cases, the buoyant layer deforms until the bifurcation point is reached (marked in red for the jet and green for the quasi-static cases, respectively), after which destabilization occurs. It is noteworthy that at destabilization, the critical height $H_c$ is roughly equivalent, but the critical length $L_c$ for the quasi-static case is more than two times larger than that for the inertial jet case.

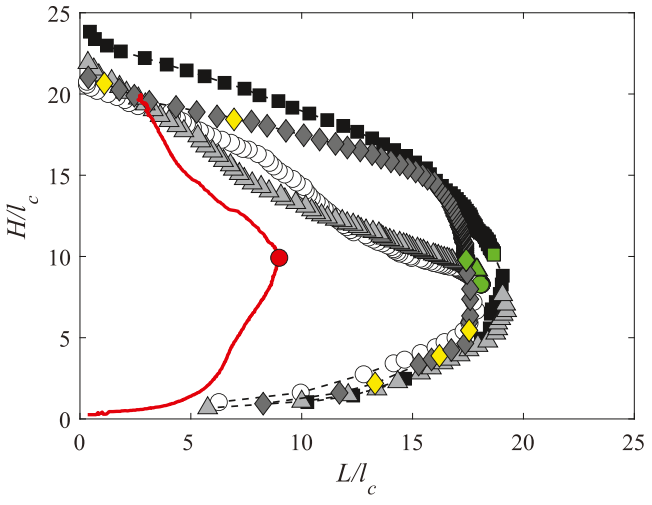


**Figure 5.** Preferred bifurcation diagram plotting the dimensionless cluster height $H/l_c$ against length $L/l_c$ for the averaged jet data (red line type) and quasi-static data (symbols) with experimental conditions corresponding to heavy particles HP3 loading a buoyant layer comprised of light particles LP1 with thickness $\delta = 3$ mm on a saline solution of 10% w/w salt concentration. For inertial jet loading, the mass flow rate is $\dot{m}_{avg} = 29.9$ g/s and funnel diameter $d_f = 8.9$ mm. The red and green symbols indicate the onset of destabilization.

The destabilization dynamics for the inertial jet case is generally repeatable, and we report the average values in Figure 5. In contrast, there is some variability for the quasi-static case, and this depends upon the location of the aforementioned protrusions. For symmetric protrusions (square and diamond symbols), the raft moves directly downward, whereas for asymmetric protrusions (circle and triangle symbols), there is an associated rotation that accompanies the downward motion giving rise to center-of-mass motion with nonzero $x$ component. Despite this variability between experiments, the critical length $L_c$ remains robust and identifiable.

We have computed the critical geometric properties of the buoyant layer $L_c$, $H_c$, $C_{y,c}$, and $A_c$ for all of our experiments and plotted these in Figure 6, distinguishing the quasi-static (grayscale line type) and inertial jet (red line type) cases. Figure 6a plots $H_c/l_c$ against $L_c/l_c$ and shows a clear delineation of the jet case, which occupies the upper left corner of the parameter space with $L_c/l_c < 9.2$ and $H_c/l_c > 6.5$. Note that a buoyant layer deformed quasi-statically can grow horizontally up to nearly 20 times its capillary length before collapsing. Interestingly, the horizontal dashed line with $H_c/l_c = 6.5$ also separates the quasi-static cases according to the density of heavy particles (black, $SG_{hp} = 3.8$, and gray, $SG_{hp} = 2.5$). This distinction does not occur for the jet case. It is worth mentioning that in all cases, the height of the buoyant layer $H_c$ is much lower than the length $L_c$, indicating that the height is the limiting factor for destabilization, in agreement with the study of Ong et al.[1] Also, note that the jet experiments have a low range of $L_c$, comparable to the funnel size, while the quasi-static ones show more variability. Lastly, we showed that the height $H_c/l_c$ correlates with the $y$-component of the center-of-mass $C_{y,c}$, as shown in Figure 6b with fits $H_c/l_c = 1.64(C_{y,c}/l_c) + 1.61$ for the jet case and $H_c/l_c = 2.25(C_{y,c}/l_c) + 0.54$ for the quasi-static case, respectively. Similarly, the nondimensional area $A_c/l_c^2$ correlates with $(C_{y,c}/l_c)^2$, as shown in Figure 6c, which allows for a much more clear distinction between the quasi-static and jet cases. We will use these correlations in the next section when developing a model to predict the load-carrying capacity of the buoyant layer.

## THEORETICAL MODEL

In this section, we develop a model to predict the critical number of heavy particles $N_c$ that causes destabilization of the buoyant layer. This involves approximating the interface shape and defining a lumped control volume, from which a force balance can be applied. Here, we generalize the analysis of Jones et al.,[27] borrowing ideas from Jambon-Puillet et al.[7] For ease of readability, we provide the detailed derivation of the mathematical model in Appendix A and simply state the main results here.

Applying a force balance to the collapsing cluster yields the governing equation


https://doi.org/10.1021/acs.langmuir.5c00012
Langmuir 2025, 41, 18403−18413

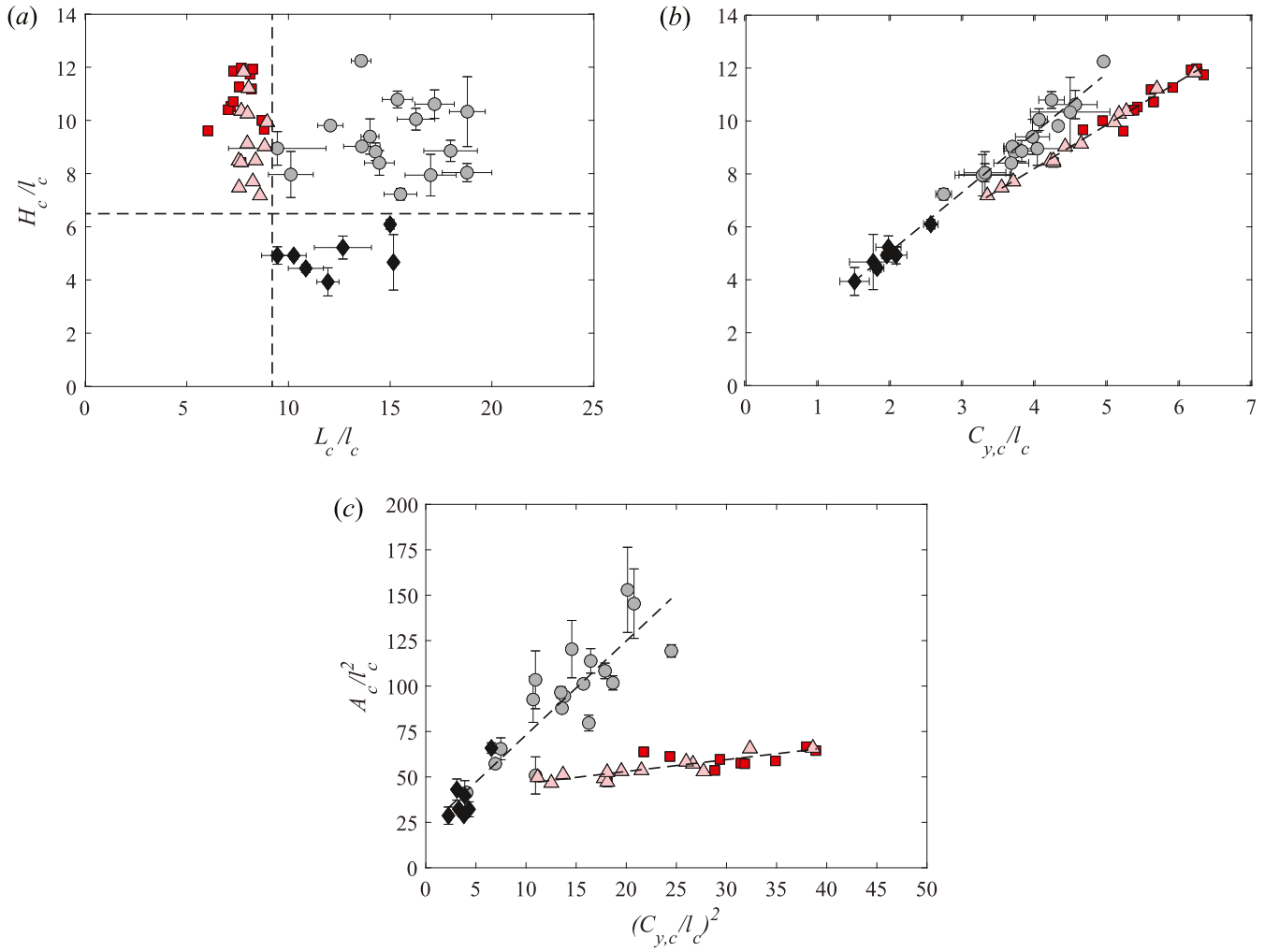


**Figure 6.** Critical cluster dimensions for the jet (red square, $SG_{hp}$ = 3.8; red triangle, $SG_{hp}$ = 2.5) and quasi-static cases (black diamond, $SG_{hp}$ = 3.8; gray circle, $SG_{hp}$ = 2.5). (a) Plotting critical depth $H_c/l_c$ against length $L_c/l_c$ separates the regions of jet impact and quasi-static loading, where the dashed lines are given by $L_c/l_c$ = 9.2 and $H_c/l_c$ = 6.5. (b,c) Correlation of the raft properties according to the loading method (jet or quasi-static) when plotting (b) height $H_c/l_c$ against the center-of-mass location $C_{y,c}/l_c$ and (c) area $A_c/l_c^2$ against $(C_{y,c}/l_c)^2$ with best fit lines $H_c/l_c = 1.64(C_{y,c}/l_c) + 1.61$, $A/l_c^2 = 0.65(C_{y,c}/l_c)^2 + 39.96$, and $H_c/l_c = 2.25(C_{y,c}/l_c) + 0.54$, $A/l_c^2 = 5.17(C_{y,c}/l_c)^2 + 21.3$, for the jet and quasi-static cases, respectively.

$$A_3x^3 + x^2 + A_1x - A_0 = 0 \tag{1}$$

for $x = N_c^{-1/3}$. Here, all nondimensional variables and parameters are absorbed into the coefficients $A_0$, $A_1$, and $A_3$, defined in (13a−13c). Note that there are three roots of (1), and for all cases discussed hereafter, we are concerned only with the largest positive real root. It will be instructive to investigate some limiting cases to (1) provide analytical predictions and (2) compare our model predictions with prior literature.

We begin with the quasi-static limit $A_3 = 0$ which yields a quadratic equation

$$x^2 + A_1x - A_0^* = 0 \tag{2}$$

where $A_0^* = A_{0,\alpha_g=0} = \left(\frac{\frac{4}{3}\Delta_{hp} - E}{2\beta\alpha_T \sin\psi \sin\phi}\right)Bo$ and has solution

$$x_1 = N_c^{-1/3} = -\frac{1}{2}Bo\left(C_1 - \sqrt{C_1^2 + 4C_0^*/Bo}\right) \tag{3}$$

where $C_0^* = A_0^*/Bo$ and $C_1 = A_1/Bo$. Equation 3 can be further simplified if the tension is solely due to the surface tension, $T_{tot} = \gamma$, as occurs for large heavy particles introduced to the interface individually.[27] Here, $\alpha_T = 1$, and (3) can be rewritten as

$$N_c = \kappa_1 Bo^{-3/2} \tag{4}$$

where $\kappa_1^{-1/3} = \frac{\sqrt{2}}{2}\sqrt{\frac{\frac{4}{3}\Delta_{hp} - E}{\beta \sin\psi \sin\phi}}$. This prediction recovers the scaling law $N_c \sim Bo^{-3/2}$ found by Jones et al.[27] A similar scaling law is predicted when capillary forces dominate, i.e., $Bo \ll 1$

$$N_c = \kappa_2 Bo^{-3/2} \tag{5}$$

where $\kappa_2^{-1/3} = \frac{\sqrt{2}}{2}\sqrt{\frac{\frac{4}{3}\Delta_{hp} - E}{\beta\alpha_T \sin\psi \sin\phi}}$.

The last special case that we consider is where heavy grains are introduced directly to a liquid/gas interface without any buoyant layer ($\delta = 0$). In this case, the tension is a function of position on the raft.[32] Here, $b = d_{hp}$ with



https://doi.org/10.1021/acs.langmuir.5c00012
Langmuir 2025, 41, 18403−18413

**Table 3. Model Parameters**

| | $\alpha_T$ | $\Phi$ | $\phi$ (°) | $\psi$ (°) | $\beta$ | $\alpha_R$ | $\alpha_L$ | $\alpha_{h,1}$ | $\alpha_{h,2}$ | $\alpha_g$ | $C$ | $k$ |
|---|---|---|---|---|---|---|---|---|---|---|---|---|
| quasi-static | 7 | 0.7 | 90 | 110.5 | 1.3 | 0 | 0 | 0 | 1 | | | |
| jet | 7 | 0.7 | 90 | 173.3 | 1 | 0.3 | 2.65 | 0 | 3.65 | 1 | 1.2 | 1.39 |
| Jones et al.[27] | 1 | 0.7 | 90 | 110.5 | 1 | 0 | 0 | 0 | 0 | | | |
| Ong et al.[1] | 7 | 0.7 | 90 | 110.5 | 1.3 | 0 | 0 | 0 | 1 | | | |

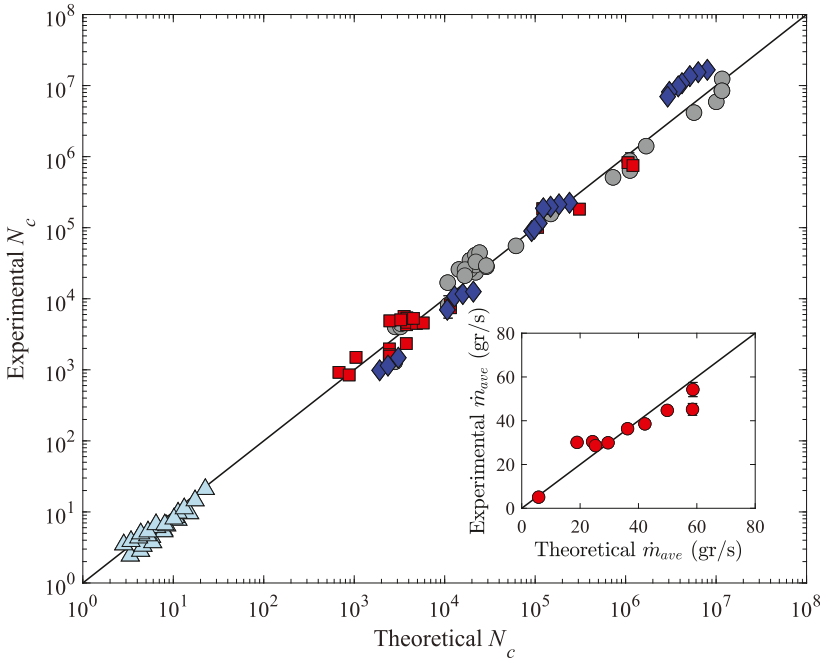


**Figure 7.** Theoretical predictions for $N_c$ compared with the current experimental jet data, squares; current experimental quasi-static data, circles; experiments of Jones et al.,[27] triangles; and those of Ong et al.,[1] diamonds. The inset shows the current experimental data for $\dot{m}_{ave}$ compared with the model of Beverloo et al.[35] (cf. eq 14).

$$A_1^* = A_{1,\delta=0} = \beta\frac{\alpha_{h,2}}{\alpha_T}(1-\Phi)Bo \tag{6}$$

giving rise to

$$N_c^{*-1/3} = -\frac{1}{2}Bo(C_1^* - \sqrt{C_1^{*2} + 4C_0^*/Bo}) \tag{7}$$

where $C_1^* = A_1^*/Bo$. We use (7) to further validate our model against the experimental data of Ong et al.[1]

We would like to compare our theoretical predictions for $N_c$ to experimental observations, but this requires us to estimate the model parameters, which we discuss in Appendix A and are summarized in Table 3. Figure 7 compares our theoretical predictions for $N_c$ to experimental observations for the quasi-static (gray circles) and inertial jet (red squares) cases. We have also added data from Jones et al.[27] (triangles) and Ong et al.[1] (diamonds) to further validate our theoretical model for low and intermediate/high values of $N_c$. The agreement between theoretical predictions and experiments is good over a large range of $N_c$. We note that the experiments of Ong et al.[1] were jet experiments with an average mass flow rate over 10 times slower than the smallest average mass flow rate used in our study and, as such, treat those data as a quasi-static case. Furthermore, their reported $N_c$ corresponds to the number of heavy particles at the collapse time, whereas for us, it signifies the onset of collapse. These slight differences have led to some deviations in comparing those experimental data with our model predictions.

## CONCLUSIONS

We conducted a set of experiments that describe the load-carrying capacity of a buoyant multilayer granular raft. Here, the loading is due to the weight of heavy grains which are introduced using two protocols, (1) quasi-static and (2) inertial jet, and are distinguished by the inertial effects of the latter. For both cases, we quantify the critical number of heavy grains $N_c$ that destabilize the raft, as it depends on a number of experimental parameters. We have also developed a mathematical model to predict $N_c$ by generalizing and extending the work of Jones et al.[27] to a buoyant multilayer raft. Our model predictions compare favorably with experimental observations over a large range of $N_c$ values (cf. Figure 7). Extensions to our model could include the incorporation of wetting effects for the particles, which influences the thickness of the wet layer through wicking. This has been demonstrated by Ong et al.,[1] who showed that the contact angle of the heavy grains influences the load-carrying capacity and collapse dynamics of a granular raft.

Finally, we note that granular rafts exhibit both continuous and discrete behaviors. At times, they behave like a solid elastic sheet, while in other instances, they act as collections of individual grains interacting through interparticle forces such as friction or forming jammed configurations when the particles come into contact. In our multilayer system, the wet layer primarily exhibits the former behavior due to capillary interactions, whereas the latter is mostly experienced by the dry layer. Also, we expect bending to influence the load-


https://doi.org/10.1021/acs.langmuir.5c00012
Langmuir 2025, 41, 18403−18413

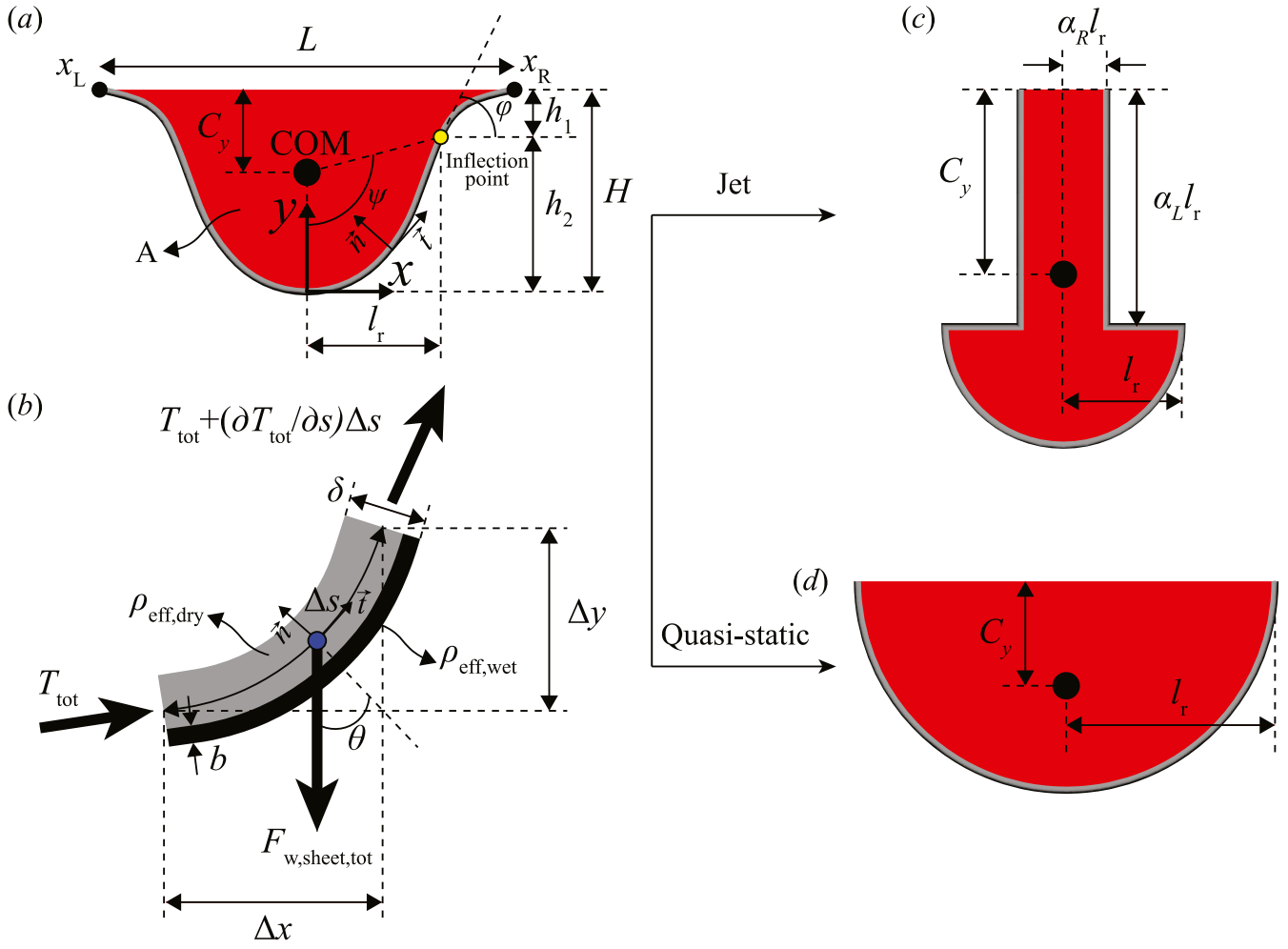


**Figure 8.** (a) Definition sketch of a deformed raft composed of multilayer buoyant particles with (b) zoomed-in control volume on an incremental arc length $\Delta s$ of the buoyant layer raft showing the unit vectors normal $\vec{n}$ and tangential $\vec{t}$ to the interface and relevant forces $F$ acting there. Destabilization will occur according to two geometries associated with (c) jet impact or (d) quasi-static pouring. Here, the $x-y$ coordinate system is placed at the minimum point, and the inflection point is denoted with a yellow filled circle.

carrying capacity more significantly in the quasi-static case, particularly in the early stages of loading before particle rearrangement occurs. To illustrate, the bending stiffness for a monolayer particle raft can be obtained from the study of Vella et al.[36] as $B \approx d_{lp}^2\gamma/[12(1-\Phi)(1+\nu)]$, where $\nu$ is the Poisson ratio of the raft. Following Vella et al., setting $\nu = 1/3$ and using the largest values for $d_{lp}$ and $\gamma$ in our experiments, we can estimate $B \approx 3 \times 10^{-8}$ N·m. We note that this bending term will appear as the fourth-order term in the classic beam equation and scales with $O(B/l_r^3 \approx B/N_c)$. Thus, the contribution of $B$ to the raft deformation becomes comparatively more important for lower $N_c$, which may explain the underestimation of $N_c$ in our quasi-static model for low $N_c$ values compared with the experiments shown in Figure 7. With regard to frictional forces, these tend to be larger for larger particles due to the increased particle-to-particle contact, and thus, less particle rearrangement is expected to occur for rafts made of larger particles.[2] These considerations support the idea that rafts composed of larger particles are more resistant to deformations and thus have a higher load-carrying capacity. Our model, however, does not account for the elastic effects or the individual interparticle forces. This should be pursued in future studies.

In a broader context, our study extends the classical water entry problem, where solid objects interact with liquid surfaces.[37,38] Here, instead of a single large object, we have considered numerous smaller heavy particles interacting with a liquid surface covered with floating particles (polystyrene), which act as a nonliquid interfacial property modifier.[39] This situation can be seen in marine environments where microplastics with sizes ranging from a few microns up to 5 mm float upon the ocean surface.[40] Here, the redistribution of particles in the liquid due to destabilization of the buoyant layer has consequences for both small- and large-scale transport of microplastics. Furthermore, high inertia interactions, such as those seen from large objects, can generate splashes, Worthington jet, and large waves that could potentially aerosolize the light particles, with associated health and environmental risks. Lastly, we note that most buoyant layers that occur in nature consist of a mixture of particles of varying sizes. We conducted preliminary tests using heterogeneous mixtures of LP1, LP2, and LP3 particles, observing that a heterogeneous layer supports a higher mass compared to a homogeneous layer. Further research is necessary to fully understand the load-carrying capacity of heterogeneous buoyant layers as well as the effect of irregularly shaped particles.


https://doi.org/10.1021/acs.langmuir.5c00012
Langmuir 2025, 41, 18403−18413

## APPENDIX A

### Derivation of the Theoretical Model

Here, we provide the details that produce the governing eq 1. We begin by considering the cluster schematically illustrated in Figure 8a, from which we can define the interface shape at the collapse time as either (1) a hemisphere with varying radius (cf. Figure 8c) or (2) a mushroom-like shape (cf. Figure 8d), consistent with experimental observations shown in Figure 3 for the quasi-static and inertial jet cases, respectively. The mushroom-like shape can be approximated as a two-body assembly composed of a cylinder connected with a hemisphere with radius $l_r$, as shown in Figure 8c. The geometry of the cylinder is defined by the half-width $\alpha_R l_r$ and length $\alpha_L l_r$. This leads to the following geometrical properties:

$$\frac{C_{y,c}}{l_r} = \frac{\alpha_L^2\alpha_R + \frac{\pi}{2}\alpha_L + \frac{2}{3}}{2\alpha_L\alpha_R + \frac{\pi}{2}} \tag{8a}$$

$$\frac{H_c}{l_r} = 1 + \alpha_L \tag{8b}$$

$$\frac{A_c}{l_r^2} = 2\alpha_L\alpha_R + \frac{\pi}{2} \tag{8c}$$

$$\beta = (1.5\alpha_L\alpha_R^2 + 1)^{-1/3} \tag{8d}$$

where $C_y$ is the vertical center-of-mass, $H$ is the total height, $A$ is the area, and $\beta$ is a volumetric shape factor. Note that $\beta$ is included here to account for interface imperfections. Setting $\alpha_L = \alpha_R = 0$ gives the limiting case of the hemispherical shape associated with the quasi-static case (cf. Figure 8d), with $C_{y,c}/l_r = 4/3\pi$, $H_c/l_r = 1$, and $A_c/l_r^2 = \pi/2$ that can be simplified to give $H_c/l_c = 2.35(C_{y,c}/l_c)$ and $A/l_c^2 = 8.72(C_{y,c}/l_c)^2$. For the jet case, we fit $\alpha_L = 2.65$ and $\alpha_R = 0.3$ to the experimental fitting lines in Figure 6 to give $H_c/l_c = 1.66(C_{y,c}/l_c)$ and $A/l_c^2 = 0.65(C_{y,c}/l_c)^2$. This defines the control volume.

We perform a force balance on the control volume (Figure 8a)

$$F_w + \dot{m}_{ave}V_{imp} - F_t - F_b = m_{com}a_{com} \tag{9}$$

Here, the weight of the control volume $F_w$ and impact inertia of the heavy particles $\dot{m}_{ave}V_{imp}$, where impact velocity $V_{imp} = \sqrt{2gD}$ with $g$ the gravitational acceleration, are destabilizing, whereas the restorative forces of tension $F_t$ and buoyancy $F_b$ are stabilizing. We assume the tension force acts on the inclination line defined as the point where the curvature of the interface shape changes sign, as shown in Figure 8a. This gives rise to an acceleration of the center-of-mass $a_{com}$ with $m_{com}$ the total mass. The functional forms of the forces are given by

$$F_w = \frac{4}{3}\pi N_c g r_{hp}^3(\rho_{hp} - \rho_{air}) \tag{10a}$$

$$F_t = 2\pi l_r T_{tot} \sin\psi \ \sin\phi \tag{10b}$$

$$F_b = \pi N_c g r_{hp}^3(\rho_l - \rho_{air})\left(-\frac{h_1}{l_r}\sin^2\psi + \frac{2}{3} - \cos\psi + \frac{1}{3}\cos^3\psi\right) \tag{10c}$$

where $h_1$ is the vertical distance between the undeformed interface and the inflection line, and the angles $\psi$ and $\phi$ define the location of the inflection line relative to the center-of-mass and the angle between the vertical direction and tangential line, respectively. Note that the buoyancy force includes the displacement of the cluster volume, as well as the contribution from the meniscus.

To determine the unknown tension $T_{tot}$, we assume the buoyant layer to be the composition of a wet layer with thickness $b$ and density $\rho_{wet}$ that is in contact with the liquid and a dry layer with thickness $(\delta - b)$ and density $\rho_{dry}$, as shown in Figure 8b.[7] The effective densities of the layers can be written as $\rho_{wet} = \rho_{lp}\Phi_1 + (1 - \Phi_1)\left(\frac{\rho_l + \rho_{air}}{2}\right)$ and $\rho_{dry} = \rho_{lp}\Phi_2 + (1 - \Phi_2)\rho_{air}$. Here, we assume the packing fractions to be equal, $\Phi_1 = \Phi_2 = \Phi$, for simplicity. Note that the total tension varies along the raft, giving rise to the term $(\partial T_{tot}/\partial s)\Delta s$, where $s$ is the arc length along the raft, and $\Delta s \approx dx\sqrt{1 + (dy/dx)^2}$ is a small increment in arc length. The total weight of the sheet is $F_{w,sheet,tot} = [\rho_{eff,wet}b + \rho_{eff,dry}(\delta - b)]g(2\pi x\Delta s)$. The tangential force balance (along $\vec{t}$ shown in Figure 8b) reads

$$dT_{tot}/dx - [\rho_{eff,wet}b + \rho_{eff,dry}(\delta - b)]g\ dy/dx = 0 \tag{11}$$

which can be integrated from $y = 0$ to $y = h_2$ to yield

$$T_{tot} = T_{tot}(0) + [\rho_{eff,wet}b + \rho_{eff,dry}(\delta - b)]gh_2 \tag{12}$$

where $T_{tot}(0)$ is the tension at the minimum of the buoyant layer profile, and $h_2$ is the distance from the inflection point to that minimum.

Substituting (10a–10c) and (12) into (9) yields the governing eq 1 presented above, with the coefficients defined as

$$A_3 = -\frac{G}{\beta\alpha_T \sin\psi \ \sin\phi} \tag{13a}$$

$$A_1 = \frac{\alpha_{h,2}}{\alpha_T}\left(\frac{\delta}{r_{hp}}\right)\beta Bo\left[\frac{b}{\delta}\left(\frac{1 - \Phi}{2}\right) + \Phi\Delta_{lp} + \Delta_{air}\right] \tag{13b}$$

$$A_0 = \frac{\frac{4}{3}[\Delta_{hp} - (\Delta_{hp} + \Delta_{air})\alpha_g] - E}{2\beta\alpha_T \sin\psi \ \sin\phi}Bo \tag{13c}$$

Here, we have assumed a characteristic length $l_r = 2^{1/3}\beta r_{hp}N_c^{1/3}$ to be the radius of a hemisphere having an equal volume as that of the falling cluster when $\beta = 1$.[27] In addition, we assume the thickness of the wet layer $b = d_{lp}$ to be that of a single light particle. Here, $\alpha_T = T_{tot}(0)/\gamma$, $\alpha_{h,1} = h_1/l_r$, $\alpha_{h,2} = h_2/l_r$, $\alpha_g = a_{com}/g$, $\Delta_{lp} = \frac{\rho_{lp} - \rho_{air}}{\rho_l - \rho_{air}}$, $\Delta_{hp} = \frac{\rho_{hp} - \rho_{air}}{\rho_l - \rho_{air}}$, $\Delta_{air} = \frac{\rho_{air}}{\rho_{lp} - \rho_{air}}$, $E = -\alpha_{h,1}\sin^2\psi + \frac{2}{3} - \cos\psi + \frac{1}{3}\cos^3\psi$, and $Bo = (r_{hp}/l_c)^2$ are all treated as constants. The parameter $G = \frac{\dot{m}_{ave}V_{imp}}{2\pi r_{hp}\gamma}$ can be simplified using the model proposed by Beverloo et al.[35] for the average mass flow rate of the heavy grains

$$\dot{m}_{ave} = C\rho_{b,hp}\sqrt{g}(d_f - kd_{hp})^{5/2} \tag{14}$$



https://doi.org/10.1021/acs.langmuir.5c00012
Langmuir 2025, 41, 18403−18413

where $\rho_{b,hp}$ is the bulk density of the heavy particles, $C$ is the empirical discharge coefficient, and $k$ is the shape coefficient, which can be determined from experimental measurements.

To compare the theoretical predictions to experimental observations, we need to estimate the model parameters which can be categorized as either geometrical parameters ($\beta$, $\psi$, $\phi$, $\alpha_{h,1}$, $\alpha_{h,2}$, $\Phi$), or dynamical parameters ($\alpha_T$, $\alpha_g$, $C$, $k$). The model parameters are summarized in Table 3.

We begin with the dynamical parameters $k = 1.39$ and $C = 1.2$ which are found from a best fit line to a plot of eq 14 against the experimental mass flow rate data, as shown in the inset of Figure 7. Here, we note that $k$ lies within the expected range ($1 < k < 2$) but that $C$ is around two times its expected value ($0.55 < C < 0.65$).[41] With regard to the geometrical parameters, we follow the work of Jambon-Puillet et al.[7] and assume $\Phi = 0.7$ for all cases, noting that our model correctly predicts the increase in load-carrying capacity with $\Phi$, consistent with the results of Planchette et al.[11] for armored puddles. For the quasi-static case, $\psi = 110.5°$, $\phi = 90°$, $\alpha_{h,1} = 0$, and $\alpha_{h,2} = 1$. For the jet case, however, considering the two-body scenario as discussed earlier gives $\psi = 173.3°$, $\phi = 90°$, $\alpha_{h,1} = 0$, and $\alpha_{h,2} = 3.65$. Note that we have set $\alpha_{h,1} = 0$ in both cases, assuming that the buoyancy contribution from the interface displacement is much smaller than that of the cluster volume.

A sensitivity analysis reveals that the parameters with the most significant impact on the system are $\beta$, which is directly related to $N_c$, and $\alpha_T$, which controls the tension $T_{tot}$. For the idealized geometries shown in Figure 8, $\beta = 1$ for the quasi-static and $\beta = 0.9$ for the jet cases, respectively. However, to account for the imperfections associated with the protrusions discussed earlier, we have set $\beta = 1.3$ for the quasi-static and $\beta = 1$ for the jet cases, respectively. Regarding the tension coefficient $\alpha_T$, Jambon-Puillet et al.[7] showed that a monolayer granular raft deformed by a liquid droplet destabilized at its base with $\alpha_T = 1.2$. Our experimental observations for a multilayer raft also support the observation that the cluster destabilizes along its inflection line; however, we find that setting $\alpha_T \approx 7$ better predicts our experimental results. The observation that $\alpha_T \approx 7$ in both the quasi-static and jet cases suggests that the raft destabilizes at its base when the tension at its minimum point reaches a certain value, independent of the inertia of the heavy grains. Finally, although we get a better fit by assuming the collapsing cluster experiences free fall $\alpha_g = 1$ at the onset of collapse, our experimental data suggest that $0.15 < \alpha_g < 0.3$.

## AUTHOR INFORMATION


### Corresponding Author

**Joshua B. Bostwick** − *Department of Mechanical Engineering, Clemson University, Clemson, South Carolina 29634, United States;* orcid.org/0000-0001-7573-2108; Phone: +1 (864) 656-5625; Email: jbostwi@clemson.edu

### Author

**Mohammad Javad Sayyari** − *Department of Mechanical Engineering, Clemson University, Clemson, South Carolina 29634, United States*

Complete contact information is available at: https://pubs.acs.org/10.1021/acs.langmuir.5c00012


### Notes

The authors declare no competing financial interest.

## ACKNOWLEDGMENTS

This work was supported by the donors of ACS Petroleum Research Fund under New Directions Grant No. 66804.

## REFERENCES


(1) Ong, X. Y.; Taylor, S. E.; Ramaioli, M. Pouring of Grains onto Liquid Surfaces: Dispersion or Lump Formation? *Langmuir* **2019**, *35*, 11150−11156.

(2) Protière, S. Particle Rafts and Armored Droplets. *Annu. Rev. Fluid. Mech.* **2023**, *55*, 459−480.

(3) Li, Z.; Tian, Q.; Hu, H. Resistance law of a rod penetrating a multilayer granular raft. *Chin. Phys. B* **2023**, *32*, 034501.

(4) Abkarian, M.; Protière, S.; Aristoff, J. M.; Stone, H. A. Gravity-induced encapsulation of liquids by destabilization of granular rafts. *Nat. Commun.* **2013**, *4*, 1895.

(5) Larmour, I. A.; Saunders, G. C.; Bell, S. E. J. Sheets of large superhydrophobic metal particles self assembled on water by the cheerios effect. *Angew. Chem., Int. Ed.* **2008**, *47*, 5043−5045.

(6) Mlot, N. J.; Tovey, C. A.; Hu, D. L. Fire ants self-assemble into waterproof rafts to survive floods. *Proc. Natl. Acad. Sci. U.S.A.* **2011**, *108*, 7669−7673.

(7) Jambon-Puillet, E.; Josserand, C.; Protière, S. Drops Floating on Granular Rafts: A Tool for Liquid Transport and Delivery. *Langmuir* **2018**, *34*, 4437−4444.

(8) Cervantes-Álvarez, A.; Escobar-Ortega, Y.; Sauret, A.; Pacheco-Vázquez, F. Air entrainment and granular bubbles generated by a jet of grains entering water. *J. Colloid Interface Sci.* **2020**, *574*, 285−292.

(9) Paume, V.; Aussillous, P.; Pouliquen, O. Finite size effects during the penetration of objects in a granular medium. *Soft Matter* **2024**, *20*, 245−254.

(10) Gabbard, C. T.; Whitesell, E. L.; Bostwick, J. B. Coat or collapse? *Phys. Rev. Fluids* **2024**, *9*, 110505.

(11) Planchette, C.; Lorenceau, E.; Biance, A.-L. Rupture of granular rafts: effects of particle mobility and polydispersity. *Soft Matter* **2018**, *14*, 6419−6430.

(12) Sanlı, C.; Lohse, D.; van der Meer, D. From antinode clusters to node clusters: The concentration-dependent transition of floaters on a standing Faraday wave. *Phys. Rev. E* **2014**, *89*, 053011.

(13) Burton, J. C.; Amundson, J. M.; Cassotto, R. K.; Kuo, C.-C.; Dennin, M. Quantifying flow and stress in ice mélange, the world's largest granular material. *Proc. Natl. Acad. Sci. U.S.A.* **2018**, *115*, 5105−5110.

(14) Hu, X.; Wei, Y.; Wang, C. Dynamic characteristics of polar ocean detector passing through the crushed ice zone based on the CFD-DEM method. *Int. J. Mech. Sci.* **2024**, *271*, 109304.

(15) Amundson, J. M.; Fahnestock, M.; Truffer, M.; Brown, J.; Lüthi, M. P.; Motyka, R. J. Ice mélange dynamics and implications for terminus stability, Jakobshavn Isbræ, Greenland. *J. Geophys. Res.: Earth Surf.* **2010**, *115*, F01005.

(16) Wehrlé, A.; Lüthi, M. P.; Vieli, A. The control of short-term ice mélange weakening episodes on calving activity at major Greenland outlet glaciers. *Cryosphere* **2023**, *17*, 309−326.

(17) Dai, C.; Higman, B.; Lynett, P. J.; Jacquemart, M.; Howat, I. M.; Liljedahl, A. K.; Dufresne, A.; Freymueller, J. T.; Geertsema, M.; Ward Jones, M.; Haeussler, P. J. Detection and Assessment of a Large and Potentially Tsunamigenic Periglacial Landslide in Barry Arm, Alaska. *Geophys. Res. Lett.* **2020**, *47*, No. e2020GL089800.

(18) Sutherland, B. R.; Balmforth, N. J. Damping of surface waves by floating particles. *Phys. Rev. Fluids* **2019**, *4*, 014804.

(19) Bailey, I.; Foster, G. L.; Wilson, P. A.; Jovane, L.; Storey, C. D.; Trueman, C. N.; Becker, J. Flux and provenance of ice-rafted debris in the earliest Pleistocene sub-polar North Atlantic Ocean comparable to the last glacial maximum. *Earth Planet. Sci. Lett.* **2012**, *341*−*344*, 222−233.

(20) Lehmann, P.; Aminzadeh, M.; Or, D. Evaporation Suppression From Water Bodies Using Floating Covers: Laboratory Studies of Cover Type, Wind, and Radiation Effects. *Water Resour. Res.* **2019**, *55*, 4839−4853.

(21) Zheng, Z.; Huppert, H. E.; Vriend, N. M.; Neufeld, J. A.; Linden, P. Flow of buoyant granular materials along a free surface. *J. Fluid Mech.* **2018**, *848*, 312−339.
(22) Hu, X.; Wei, Y.; Wang, C. Dynamic characteristics of polar ocean detector passing through the crushed ice zone based on the CFD-DEM method. *Int. J. Mech. Sci.* **2024**, *271*, 109304.
(23) Mitarai, N.; Nori, F. Wet granular materials. *Adv. Phys.* **2006**, *55*, 1−45.
(24) Saddier, L.; Palotai, A.; Aksil, M.; Tsamados, M.; Berhanu, M. Breaking of a floating particle raft by water waves. *Phys. Rev. Fluids* **2024**, *9*, 094302.
(25) Delon, G.; Terwagne, D.; Dorbolo, S.; Vandewalle, N.; Caps, H. Impact of liquid droplets on granular media. *Phys. Rev. E* **2011**, *84*, 046320.
(26) Vella, D.; Metcalfe, P. D.; Whittaker, R. J. Equilibrium conditions for the floating of multiple interfacial objects. *J. Fluid Mech.* **2006**, *549*, 215−224.
(27) Jones, S. G.; Abbasi, N.; Ahuja, A.; Truong, V.; Tsai, S. S. H. Floating and sinking of self-assembled spheres on liquid-liquid interfaces: Rafts versus stacks. *Phys. Fluids* **2015**, *27*, 072102.
(28) Ong, X. Y.; Taylor, S. E.; Ramaioli, M. On the formation of dry granular jets at a liquid surface. *Chem. Eng. Sci.* **2021**, *245*, 116958.
(29) Sano, T. G.; Hayakawa, H. Simulation of granular jets: Is granular flow really a perfect fluid? *Phys. Rev. E* **2012**, *86*, 041308.
(30) Shi, Z.-H.; Li, W.-F.; Qian, W.-W.; Liu, H.-F.; Wang, F.-C. Liquid-like granular film from granular jet impact. *Chem. Eng. Sci.* **2017**, *162*, 1−9.
(31) Pasandideh-Fard, M.; Qiao, Y. M.; Chandra, S.; Mostaghimi, J. Capillary effects during droplet impact on a solid surface. *Phys. Fluids* **1996**, *8*, 650−659.
(32) Protière, S.; Josserand, C.; Aristoff, J. M.; Stone, H. A.; Abkarian, M. Sinking a Granular Raft. *Phys. Rev. Lett.* **2017**, *118*, 108001.
(33) Raux, P. S.; Cockenpot, H.; Ramaioli, M.; Quéré, D.; Clanet, C. Wicking in a Powder. *Langmuir* **2013**, *29*, 3636−3644.
(34) Wang, M.-K.; Yang, G.-H.; Zhang, S.; Cai, H.-J.; Lin, P.; Chen, L.-W.; Yang, L. A numerical study of dynamics in thin hopper flow and granular jet. *Chin. Phys. B* **2020**, *29*, 048102.
(35) Beverloo, W.; Leniger, H.; van de Velde, J. The flow of granular solids through orifices. *Chem. Eng. Sci.* **1961**, *15*, 260−269.
(36) Vella, D.; Aussillous, P.; Mahadevan, L. Elasticity of an interfacial particle raft. *Europhys. Lett.* **2004**, *68*, 212.
(37) Aristoff, J. M.; Bush, J. W. M. Water entry of small hydrophobic spheres. *J. Fluid Mech.* **2009**, *619*, 45−78.
(38) Truscott, T. T.; Epps, B. P.; Belden, J. Water Entry of Projectiles. *Annu. Rev. Fluid. Mech.* **2014**, *46*, 355−378.
(39) Watson, D. A.; Anzola, S.; Zeas, F. A.; Smith, K. B.; Cruz, A. A. Compound cavity formation and splash crown suppression by water entry through proximally adjacent polystyrene beads. *Phys. Fluids* **2024**, *36*, 092124.
(40) Shamskhany, A.; Li, Z.; Patel, P.; Karimpour, S. Evidence of microplastic size impact on mobility and transport in the marine environment: a review and synthesis of recent research. *Front. Mar. Sci.* **2021**, *8*, 760649.
(41) Mankoc, C.; Janda, A.; Arévalo, R.; Pastor, J. M.; Zuriguel, I.; Garcimartín, A.; Maza, D. The flow rate of granular materials through an orifice. *Granul. Matter* **2007**, *9*, 407−414.


https://doi.org/10.1021/acs.langmuir.5c00012
*Langmuir* 2025, 41, 18403−18413